Generalized theory of helicon waves. II. Excitation and absorption

Donald Arnush[a] and Francis F. Chen
Electrical Engineering Department, University of California, Los Angeles, Los Angeles, California 90095-1594

(Received 17 June 1997; accepted 3 February 1998)

Helicon waves in a plasma confined by a cylinder are treated. The undamped normal modes of the helicon (H) and Trivelpiece–Gould (TG) waves have distinctly different wave patterns at high magnetic fields but at low fields have similar patterns and therefore interact strongly. Damping of these modes, their excitation by antennas, and the rf plasma absorption efficiency are considered. Nonuniform plasmas are treated by solving a fourth-order ordinary differential equation numerically. A significant difference between this and earlier codes which divide the plasma into uniform shells is made clear. Excitation of the weakly damped H wave, followed by conversion to the strongly damped TG wave which leads to high helicon discharge efficiency, is examined for realistic density profiles. A reason for the greater heating efficiency of the $m=+1$ vs the $m=-1$ mode for axially peaked profiles is provided. © *1998 American Institute of Physics.* [S1070-664X(98)02505-1]

I. INTRODUCTION

In Part I of this work,[1] which we rely on for the definition of common terms, the undamped normal modes in a uniform, cylindrical plasma for

$$\omega_{\mathrm{LH}} \ll \omega \ll \omega_{ce} \ll \omega_{pe} \tag{1}$$

are identified as helicon (H) and Trivelpiece–Gould (TG) waves, and their properties and interactions were discussed. In Part II we discuss the excitation, by an external antenna, of coupled H and TG waves in a radially nonuniform, collisional plasma. Though the antenna is finite in length, the plasma is infinitely long, and the entire system is bounded by a concentric conducting cylinder.

In the uniform-density case, H waves penetrate to the center of the plasma but are very weakly damped by collisions, and hence are an unlikely channel for the strong rf absorption observed in helicon plasmas.[2] In order to meet the boundary conditions TG waves must be present at the plasma surface. The required TG field amplitudes are usually small and hence are hard to measure, but their currents, which are proportional to $\nabla \times \mathbf{B}$, can be quite large because their transverse wave number is typically much larger than for the H waves. Large net currents then occur which are strongly damped by collisions. Usually, the energy deposition occurs primarily near the surface, since the TG amplitudes decrease rapidly away from the antenna. This mechanism of absorption via mode coupling was pointed out by Shamrai *et al.*[3] but was treated only in uniform plasmas. Further discussion of the results of neglecting TG waves is provided at the end of Sec. III.

For a nonuniform plasma with a more realistic density profile, coupling between the H and TG waves occurs throughout the plasma volume, resulting in more uniform heating. Inclusion of the density gradient terms results in a fourth-order differential equation for the wave fields which must be solved numerically. Many previous authors treated antenna coupling without considering the TG waves,[2,4] thereby missing their critical contributions. Other authors approximated the density variation with a series of constant-density shells.[5,6] In doing this, they used the exact constant-density solution in each shell and required that the fields be continuous at the interfaces, thus neglecting the charges and currents there. In this work, we derive analytic expressions for the density-gradient terms and find that these terms are essential to the mode-coupling mechanism (our results reproduce those of previous authors[7] when TG waves may be neglected). These effects could have been included in the shell model if the proper boundary conditions had been used. In Sec. IV, we give numerical results illustrating the difference between our result and that obtained by using, for example, the approach used in the ANTENNA code.[5,6] We also explore the moderate magnetic field in detail. In Sec. V, a summary of our main conclusions is presented.

In this paper, the problem is divided into two parts. In Sec. II, the antenna currents are related to the fields on the plasma surface; in Sec. III, these surface fields are related to those in the interior by using the cold-plasma dielectric representation of the plasma. Finite-temperature effects in the direction parallel to the dc magnetic field $\mathbf{B}_0$, such as Landau damping, can be included by using a kinetic form of the dielectric element ϵ_{zz};[8] but since the equilibrium configuration is nonuniform in the radial direction, such kinetic effects as finite Larmor radius cannot be readily included. For relatively flat density profiles, this method of solution enables us to distinguish the H and TG waves and thus to compare our results to those obtained by more approximate methods. Solving the plasma equations is by far the most time-consuming part of the computation. Once that is done, we may rapidly explore a wide variety of antenna designs using the relationship of the antenna currents to the plasma surface fields to optimize the coupling.

[a]Electronic mail: darnush@ucla.edu

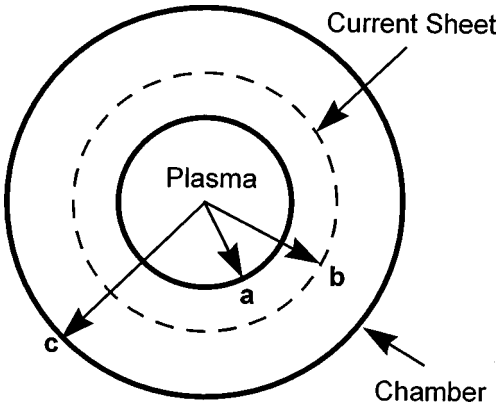

FIG. 1. The modeled configuration.

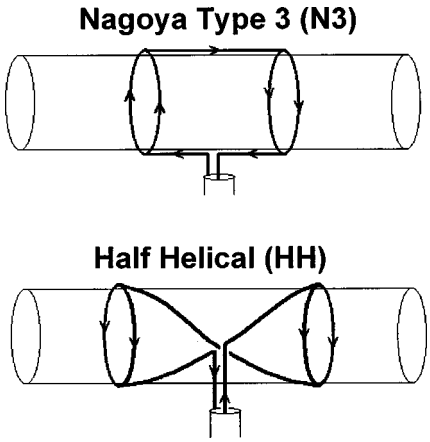

FIG. 2. Two of the antennas investigated.

As an illustration of the method we shall explore in detail the following representative case:

$$n_0=10^{12}\ \text{cm}^{-3},\quad N_{\text{Ar}}=10^{14}\ \text{cm}^{-3},\quad T_e=3\ \text{eV},\qquad B_0=100\ \text{G},\quad a=4\ \text{cm},\quad f=13.56\ \text{MHz} \tag{2}$$

(where n_0 is the plasma density on the axis and a is the plasma radius) for a variety of density profiles, antennas, and azimuthal mode numbers m. The antenna wires are assumed to lie on a cylinder of radius b, and a conducting wall of radius c surrounds the system, as shown in Fig. 1; but, as we shall show, the major physical effects present in most experiments can be adequately illustrated by taking $b=a$ and $c\to\infty$. For fields B_0 higher than about 800 G, the numerical computations become cumbersome, and for those cases we have devised a more convenient method, which will be presented in a subsequent publication. Note that the plasma parameters are assumed given; the problem of discharge equilibrium, in which the density profiles and thermal distributions are found self-consistently, is not considered here.

II. ANTENNA-COUPLING

The plasma and conducting cylinder surrounding it are assumed to be uniform in the azimuthal (ϕ) and axial (z) directions, where z is the direction of $\mathbf{B}_0$. We can therefore use Fourier transforms in these directions. We assume that the system is sufficiently long, and the k spectrum sufficiently dense, to use a Fourier integral in the z direction. Each component of an arbitrary vector $\mathbf{V}$ is then given by

$$\underline{V}_j(r,\phi,z)=\frac{1}{2\pi}\int_{-\infty}^{\infty}dk\sum_{m=-\infty}^{\infty}V_j(r,m,k)e^{i(m\phi+kz)}, \tag{3}$$

where

$$V_j(r,m,k)=\int_{-\infty}^{\infty}dz\int_0^{2\pi}\frac{d\phi}{2\pi}\,\underline{V}_j(r,\phi,z)e^{-i(m\phi+kz)}. \tag{4}$$

The underline denotes field quantities in real space. The antenna current density has the form $\underline{\mathbf{J}}(r,\phi,z)=\delta(r-b)\underline{\mathbf{K}}(\phi,z)$ and the Fourier transform of $\underline{\mathbf{K}}(\phi,z)$ is $\mathbf{K}(m,k)$. We assume that the electrostatic fields are shielded from the plasma so that

$$\nabla\cdot\underline{\mathbf{J}}=0$$

and hence

$$K_z(m,k)=-\frac{m}{bk}K_\phi(m,k). \tag{5}$$

Though the formalism is general, we confine our attention to $m=0$, $+1$, and -1 waves excited by the simple loop antenna, the two antennas shown in Fig. 2, and a single-turn double helix. For I_0 amperes the transform for a loop is $K_\phi=I_0$ for $m=0$, and zero otherwise. For helices the transforms are zero for m even, and for m odd are—fractional helix:

$$K_\phi=-\frac{2}{\pi}I_0\frac{kL}{2m}\frac{\sin\left(\frac{kL}{2}-m\theta\right)}{\frac{kL}{2}-m\theta}, \tag{6a}$$

integral t-turn helix:

$$K_\phi=2I_0\left[\frac{\sin\left(\frac{kL}{2t}-\pi m\right)}{\frac{kL}{2t}-\pi m}\sum_{j=1}^{t}e^{i(kL/2t)(t+1-2j)}-\frac{\sin\left(\frac{kL}{2}\right)}{\pi m}\right], \tag{6b}$$

where L is the antenna length and θ is half the twist angle from one end to the other. The k dependence of $|K_\phi|^2$, proportional to antenna power, is shown in Fig. 3 for an $m=1$ Nagoya Type III (N3, $\theta=0$), a half-helical (HH, $\theta=\pi/2$), and a one-turn helical (H1, $t=1$) antenna. Their lengths are 0.12, 0.20, and 0.30 m, respectively, selected to maximize $|K_\phi|^2$ at $k=26\ \text{m}^{-1}$ for each. For these values the antenna spectra have a forward-to-back peak power ratio of about 1:1, 10:1, and 34:1, respectively.

For perturbations varying as $\exp[i(m\phi+kz-\omega t)]$ in a radially nonuniform plasma, Maxwell's equations can be written as

$$\nabla\times\mathbf{E}=i\omega\mathbf{B}$$
$$\nabla\times\mathbf{B}=-i(\omega/c^2)\mathscr{E}(r)\cdot\mathbf{E}. \tag{7}$$

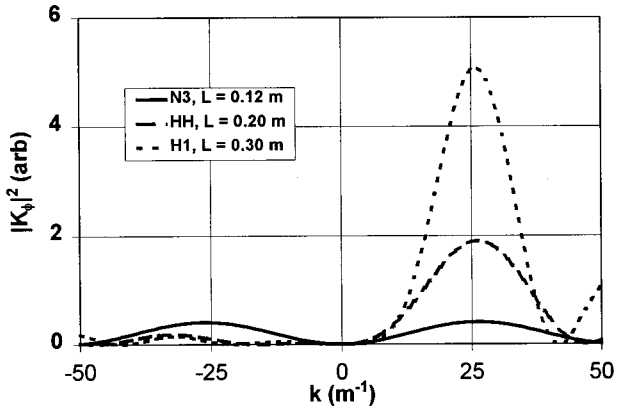

FIG. 3. Power spectrum (arbitrary units) for the $m=1$ component of three antennas. Positive k corresponds to the direction of $\mathbf{B}_0$.

With the two divergence constraints, these constitute four scalar equations which can be reduced to a fourth-order ordinary differential equation (ODE) for any field component (see Sec. III). For a nonsingular density profile there are four independent solutions, of which two are singular at the origin. There are therefore two independent sets of physical basis functions, which we denote by lower case letters and the subscripts 1 and 2. For a constant density profile they are the H and TG modes described using Bessel functions in Part I.[1] For arbitrary density profiles, these basis functions have to be found numerically. As the density profile is gradually distorted to approach a more realistic shape, the solutions gradually become transformed. For each component V_i of any wave quantity (e.g., **E**, **B**, or **J**) we have

$$V_i = A_1 v_{1,i} - A_2 v_{2,i}, \tag{8}$$

with amplitudes A_1 and $-A_2$ to be determined. For instance,

$$E_r = A_1 e_{1,r} - A_2 e_{2,r}, \quad B_\phi = A_1 b_{1,\phi} - A_2 b_{2,\phi}, \quad \text{etc.} \tag{9}$$

In vacuum, the basis functions are $K_m(Tr)$ and $I_m(Tr)$, with $T^2 = k^2 - k_0^2$, where $k_0 \equiv \omega/c$. Since there are two vacuum regions (plasma–antenna and antenna–wall), with two basis functions and two waves [transverse-electric (TE) and transverse-magnetic (TM)] in each, there are eight coefficients to be determined there. Together with A_1 and A_2 in the plasma, we have a total of ten unknown constants to describe the fields. The tangential electric field is continuous at the three boundaries, yielding six conditions. The tangential magnetic field is continuous at the plasma surface but undergoes a jump across the antenna shell. There are therefore ten boundary conditions to determine the ten unknown constants. These algebraic equations are readily solved, and the result is conveniently expressed in the following form:

$$V_i(r) = \frac{H_2 v_{1,i}(r) - H_1 v_{2,i}(r)}{D(a,c,k)} K_\phi, \tag{10}$$

where

$$\begin{aligned} D(a,c,k) &= F_1 G_2 - F_2 G_1, \\ F_n &= -ib_{n,r}(a) + \frac{k}{T} p_m(a) b_{n,z}(a) \\ &\quad - i \frac{m}{aT^2} \mu_0 [\omega \epsilon_0 e_{n,z}(a)], \\ G_n &= j_{n,r}(a) + i \frac{m}{a} \frac{k_0^2}{T^2} \frac{1}{\mu_0} b_{n,z}(a) + \frac{k}{T} q_m [\omega \epsilon_0 e_{n,z}(a)], \\ H_n &= \frac{kb}{Ta} p_m(b) \mu_0 G_n - i \frac{m}{a} \frac{k_0^2}{T^2} \rho_m F_n, \end{aligned} \tag{11}$$

and

$$\begin{aligned} p_m(r) &= \frac{K_m'(Tr) I_m'(Tc) - K_m'(Tc) I_m'(Tr)}{K_m(Ta) I_m'(Tc) - K_m'(Tc) I_m(Ta)}, \\ q_m &= \frac{K_m'(Ta) I_m(Tc) - K_m(Tc) I_m'(Ta)}{K_m(Ta) I_m(Tc) - K_m(Tc) I_m(Ta)}, \\ \rho_m &= \frac{K_m(Tb) I_m(Tc) - K_m(Tc) I_m(Tb)}{K_m(Ta) I_m(Tc) - K_m(Tc) I_m(Ta)}. \end{aligned} \tag{12}$$

Here the subscript n is 1 for the H-like wave and 2 for the TG-like wave, m is the azimuthal mode number, $b_{n,i}$, $e_{n,i}$, and $j_{n,i}$ are the basis functions for the magnetic and electric fields and the current, and the prime ($'$) stands for differentiation with respect to the argument of the Bessel function.

We see from Eq. (10) that the solution is composed of three parts. First, the fields are proportional to the Fourier transform K_ϕ of the antenna current. Second, they are inversely proportional to the dispersion function D, which is independent of the antenna properties. In the absence of damping, the equation $D=0$ gives precisely the dispersion relation for coupled H and TG modes discussed in Part I. Third, the numerator of Eq. (10) gives the radial variation of the fields and consists of the basis functions multiplied by the amplitudes H_i, which depend only on the values of the fields on the plasma surface and on the geometric functions p, q, and ρ. Once the basis functions have been computed for a given density profile, the evaluation of Eq. (10) can be completed rapidly for any antenna configuration.

Application of the boundary conditions can easily be carried out numerically without approximation. However, to elucidate the transition between conducting and insulating boundary conditions, we now explore the consequences of neglecting the displacement current. In most cases of interest, we have $k_0 \ll k$ and T, and consequently may neglect the displacement current in square brackets in Eqs. (11) for F_n and G_n, as well as the terms containing k_0^2 in G_n and H_n. We then have $H_n \propto G_n \propto j_{n,r}$ and Eqs. (10) and (11) can be simplified considerably as follows:

$$\begin{aligned} V_i(r) &= \frac{j_{2,r}(a) v_{1,i}(r) - j_{1,r}(a) v_{2,i}(r)}{D(a,c,k)} \\ &\quad \times \left(\frac{bk}{a|k|} p_m(a,b,c,k) \mu_0 K_\phi \right), \end{aligned} \tag{13}$$

where

$$p_m(a,b,c,k)\equiv p_m(b), \quad G_n=j_{n,r}(a),$$
$$F_n=-ib_{n,r}+\frac{k}{|k|}\,p_m(a,a,c,k)b_{n,z}. \tag{14}$$

From Eq. (13), we see now that the insulating-boundary condition $J_r(a)=0$ is automatically satisfied. Furthermore, the condition for antiresonance (i.e., the production of a pure H or pure TG waves) can be generalized to

$$j_{n,r}(a)=0. \tag{15}$$

This is equivalent to the Shamrai *et al.*[3] result for constant density $b_{n,r}(a)=0$, since for that case $\mu_0\mathbf{j}_n=\beta_n\mathbf{b}_n$, where β_n is the total wave number (see Part I).

The approximations which reduce Eq. (13) to its greatly simplified form fail in the limit that the gap, $d=c-a$, between the plasma and the wall approaches zero. The function q_m then approaches infinity and cancels from the numerator and denominator of Eq. (10) as $G_n,H_n\to\infty$. In that limit the numerator of Eq. (10) is the same as the numerator of Eq. (13) with $j_{n,r}(a)$ replaced by $e_{n,z}(a)$, ensuring that $E_z(a)=0$. Net radial currents are then closed by the conducting shell. For a very thin gap the radial currents also need not vanish at the plasma surface as for an ideal insulating boundary, since they can be carried to the conducting shell by displacement currents in the gap. In that case, we take the limit $c\to a$ and expand q_m in powers of d to find that we may neglect the displacement curernt contribution to G_n for kd much larger than the ratio of the axial displacement current to the radial current at the surface, i.e., for

$$kd\gg\frac{\omega\epsilon_0 e_{n,z}}{j_{n,r}}\to\frac{\omega\omega_c}{\omega_p^2}=\frac{k_0^2}{k_w^2}, \tag{16}$$

where the arrow denotes the approximate value of the expression for a constant density profile. As defined in Part I, k_w is the whistler wave number in an unbounded medium. Equation (16) is satisfied except for very small gaps. Equations (13) and (14) were used in the computations that follow, since Eq. (16) is well satisfied for the parameters used.

In Part I we found that, when a uniform, collisionless plasma is in contact with a conducting boundary, the H and TG waves can satisfy the boundary conditions independently, since the E_z condition is automatically satisfied. Shamrai *et al.*[3] have pointed out that the H and TG modes are decoupled if $d=c-a<d_{\rm crit}$. We can now generalize their result by first rewriting the dispersion function in the form

$$D=-i(b_{1,r}j_{2,r}-b_{2,r}j_{1,r})+p_m(a,a,c,k)(b_{1,z}j_{2,r}-b_{2,z}j_{1,r}). \tag{17}$$

From Eq. (12), we find that for $d\ll 1/k\leqslant a$, $p_m(a,a,c,k)$ has the following limit:

$$|p_m(a,a,c,k)|\to|-(1+m^2/k^2a^2)kd|\ll 1, \tag{18}$$

allowing us to neglect the last two terms in Eq. (17). If, furthermore, $k\gg k_{\rm min}=2k_w\sqrt{\delta_r}$, where $\delta_r=\omega/\omega_c$, the transverse wave number of the TG wave greatly exceeds that of the H wave. Since $\mathbf{j}_n$ depends on $\mathbf{b}_n$ roughly as $\mu_0\mathbf{j}\approx\beta\mathbf{b}$, the second term in Eq. (17) is much smaller than the first term, and we obtain for d sufficiently small

$$D\cong -ib_{1,r}j_{2,r}. \tag{19}$$

Consequently the dispersion relation factors and the H and TG waves are decoupled for small gaps d. For a constant density profile the condition on d can be estimated as

$$\frac{d}{a}\ll\frac{k^2}{k_w^2}\left(\frac{ka}{m^2+k^2a^2}\right), \tag{20}$$

which reproduces the Shamrai *et al.*[3] criterion for decoupling the modes. The right-hand side of Eq. (20) increases monotonically with k. Substituting $k_{\rm min}$ for k, we find that for the parameters of Eq. (2), for example, Eq. (20) requires that $d/a\ll 0.1$ for the modes to decouple.

III. PLASMA FIELD CALCULATION

We now compute the basis vector **b** (**e** and **j** are readily derived from **b** using Maxwell's equations) for plasmas with arbitrary radial density variations. In Part I we inverted the dielectric tensor to obtain **E** as a function of **J**. Eliminating **E** and **J** from Maxwell's equations, we obtain

$$k_0^2\mathbf{B}=\boldsymbol{\nabla}\times\{\alpha_c\boldsymbol{\nabla}\times\mathbf{B}+i\alpha_h\hat{\mathbf{z}}\times(\boldsymbol{\nabla}\times\mathbf{B}) + \alpha_d\hat{\mathbf{z}}\times[\hat{\mathbf{z}}\times(\boldsymbol{\nabla}\times\mathbf{B})]\}. \tag{21}$$

In the Appendix, Eq. (21) is reduced to a fourth-order ODE for the general case. Here we derive the result for the much simpler case relevant to most laboratory helicon waves by neglecting ion motions and displacement currents. Following Part I, we have

$$\alpha_h=\omega\omega_c/\omega_p^2=k_0^2/k_w^2, \quad \alpha_c=-\alpha_h\delta, \quad \alpha_d=0, \tag{22}$$

where the α's now vary with radius. Using

$$\boldsymbol{\nabla}\times[\hat{\mathbf{z}}\times(\boldsymbol{\nabla}\times\mathbf{B})]=-ik(\boldsymbol{\nabla}\times\mathbf{B}), \tag{23}$$

we obtain

$$\delta\boldsymbol{\nabla}\times\boldsymbol{\nabla}\times\mathbf{B}-k\boldsymbol{\nabla}\times\mathbf{B}+k_w^2\mathbf{B} =u(r)[-\delta_0\hat{\mathbf{r}}\times(\boldsymbol{\nabla}\times\mathbf{B})+i(\boldsymbol{\nabla}\times\mathbf{B})_r\hat{\mathbf{z}}], \tag{24}$$

where

$$\delta=\frac{\omega}{\omega_c}\left(1+i\,\frac{\nu_{en}+\nu_{ei}}{\omega}\right), \quad \delta_n=\frac{\omega}{\omega_c}\left(1+i\,\frac{\nu_{en}}{\omega}\right),$$
$$u(r)=\frac{\alpha_h'}{\alpha_h}=-\frac{n_0'(r)}{n_0(r)}. \tag{25}$$

Note that δ_* of Part I has been replaced by δ. For constant density, $u(r)$ vanishes, and Eq. (24) reduces to Eq. (10) of Part I. If the plasma is divided into constant-density shells, the terms proportional to $u(r)$ become delta functions at the interfaces, representing charges and currents accumulating there from charged-particle motions along the magnetic field. The resulting jumps in boundary values are neglected in codes such as the ANTENNA code.[5,6] These effects can be evaluated simply by comparing the solution of Eq. (24) to

that obtained by neglecting its right-hand side. To solve Eq. (24), we first write the r component and eliminate B_z using $\nabla \cdot B = 0$. The result is

$$B_r'' = \left[\frac{m}{r\delta} - \frac{1}{r}\right] B_r' + \left[k^2 + \frac{1+m^2}{r^2} + \frac{k_w^2}{\delta} + \frac{m}{r^2\delta}\right] B_r + \left[\frac{2m}{r^2} + \frac{1}{\delta}\left(k^2 + \frac{m^2}{r^2}\right)\right] \tilde{B}_\phi, \tag{26}$$

where $\tilde{B}_\phi = iB_\phi$. Next, we write the ϕ component of Eq. (21) and eliminate first B_z and then B_r'' using Eq. (26) to obtain

$$\tilde{B}_\phi'' = -\left[\frac{k_w^2}{\delta^2} + \frac{m\delta_0}{r\delta}\, u + \frac{1}{r^2}\left(\frac{m^2}{\delta} + \frac{m}{\delta^2} - 2m\right)\right] B_r - \frac{m}{r\delta^2}\, B_r' + \left[k^2\left(1 - \frac{1}{\delta^2}\right) + \frac{k_w^2}{\delta} - \frac{\delta_0 u}{r\delta} + \frac{1}{r^2} \times \left(1 + m^2 - \frac{m}{\delta} - \frac{m^2}{\delta^2}\right)\right] \tilde{B}_\phi - \left[\frac{1}{r} + \frac{\delta_0}{\delta}\, u + \frac{m}{r\delta}\right] \tilde{B}_\phi'. \tag{27}$$

Note that by solving Eq. (26) for B_ϕ and substituting it in Eq. (27) we get a fourth-order ODE for B_r. The equations are invariant for $k \to -k$ but not for $m \to -m$. It is therefore sufficient to integrate the equations only for positive k for each m. The nonsingular solutions to Eqs. (26) and (27) are denoted $\mathbf{b}_1$ and $\mathbf{b}_2$, distinguished by their behavior near the axis. The integration of the equations begins at the first radial step from the origin where two different sets of values and derivatives are used which correspond to the H and TG solutions for a uniform plasma on the axis. Two independent solutions are thereby assured which would reduce to the usual H and TG solutions if a flat density profile were chosen.

The power transferred to the plasma is

$$P = \frac{1}{2}\int \mathbf{E}^* \cdot \mathbf{J}_{\text{plasma}} d^3r = \frac{|I_0|^2}{2}\,(R_A + iX_A), \tag{28}$$

where the integral is over the plasma volume, R_A is the antenna plasma resistance, and X_A its reactance. It differs from the antenna resistance,[8] proportional to half the volume integral of $\mathbf{E}^* \cdot \mathbf{J}_{\text{antenna}}$, by the flux of wave power escaping from the cylinder at infinity and is directly relevant to calculations of the plasma equilibrium. For plasmas which satisfy the conditions of Eq. (1) we express the electric field in terms of the current as in Eq. (13) of Part I and integrate Eq. (28) to obtain the power distribution as a function of r or z, for 1 A of antenna current. Defining $P_\pm(r,m)\Delta r$ to be the power absorbed in an axially infinite, cylindrical shell of radius r and thickness Δr, from waves of mode m traveling in the $\pm z$ direction, and $P_z(z,m)\Delta z$ to be the power absorbed in a plasma cross section of thickness Δz at the location z, we have:

$$P_\pm(r,m)\Delta r = \pm\frac{\mu_0}{2}\,\frac{\omega}{\omega_c}\,\frac{\nu(r)}{k_w^2(r)} \int_0^{\pm\infty} dk\, |\mathbf{J}(r,m,k)|^2 \Delta r,$$

$$P_r(r,m) = P_+(r,m) + P_-(r,m), \tag{29}$$

$$P_z(z,m)\Delta z = \frac{\pi\mu_0}{2}\,\frac{\omega}{\omega_c} \int_0^a r dr\, |\underline{\mathbf{J}}(r,m,z)|^2\, \frac{\nu(r)}{k_w^2(r)}\, \Delta z.$$

The antenna plasma resistance and the part due to each m mode are:

$$R_A(m) = R_+(m) + R_-(m), \qquad R_\pm(m) = 2\int_0^a r dr P_\pm(r,m). \tag{30}$$

Similarly, the reactance is

$$X_A = \frac{-\mu_0\omega}{|I_0|^2} \sum_{m=-\infty}^{\infty} \int_0^a \frac{r dr}{k_w^2(r)} \int_{-\infty}^{\infty} dk \left[\frac{\omega}{\omega_c}\,|\mathbf{J}|^2 - i\hat{\mathbf{z}}\cdot(\mathbf{J}\times\mathbf{J}^*)\right] = \frac{-\mu_0\omega/\omega_c}{|I_0|^2} \sum_{m=-\infty}^{\infty} \int_0^a \frac{r dr}{k_w^2(r)} \int_{-\infty}^{\infty} dk \left[\frac{\omega}{\omega_c}\,|\mathbf{J}|^2 + 2\,\mathrm{Re}(J_r \tilde{J}_\phi^*)\right]. \tag{31}$$

It is also useful, particularly for calculating the optimal antenna length, to define a spectral antenna plasma resistance $P_k(k,m,L)$ and factor it into the ''specific'' (i.e., independent of antenna) power density S_k and antenna power density p_A as follows:

$$R_A(m,L) = \int_{-\infty}^{\infty} dk P_k(k,m,L) = \int_{-\infty}^{\infty} dk S_k(k,m) p_A(k,m,L),$$

$$S_k(k,m) = \mu_0\,\frac{\omega}{\omega_c}\left|\frac{b p_m(a,b,c,k)}{a D(a,c,k)}\right|^2 \int_0^a r dr |j_{2,r}(a)\mathbf{j}_1(r) - j_{1,r}(a)\mathbf{j}_2(r)|^2\, \frac{\nu(r)}{k_w(r)}, \tag{32}$$

$$p_A(k,m,L) = \frac{1}{I_0^2}\,|K_\phi(k,m,L)|^2.$$

Rearranging Eq. (13) for $V_i = J_i$, for example, it is now possible to make some general comments about the effects of neglecting TG waves by setting $E_z = 0$ and including only the Hall terms[2,4] D (i.e., $m_e = 0$) or the Hall and transverse field diagonal terms[9] S in the dielectric tensor (i.e., m_e finite but $P \to \infty$). This will facilitate the comparison of our results with those of previous authors.[2,9,8] The general expression is

$$\mathbf{J}(r) = \frac{bk}{a|k|}\,\frac{p_m(a,b,c,k)\mu_0 K_\phi}{F_1 - \Gamma_m(a) j_{1,r}(a)} \times \left(\mathbf{j}_1(r) - j_{1,r}(a)\,\frac{\mathbf{j}_2(r)}{j_{2,r}(a)}\right), \tag{33}$$

where

$$\Gamma_m(a) = \frac{F_2}{j_{2,r}(a)}. \tag{34}$$

Repeating the derivation of Eq. (13) assuming $E_z=0$, we obtain the same result but without the terms proportional to $\Gamma_m(a)$ and $j_{1,r}(a)$ in Eq. (33). Thus, the transverse electric assumption along with the antiresonance condition, which in this case is the same as the insulating boundary condition, results in the same field shapes as those predicted here but with amplitudes modified by the additional term in the spatially constant denominator. At high magnetic field, δ approaches zero, Eq. (24) becomes singular, and Eqs. (26) and (27) become redundant. In this limit the surviving set of solutions describe the helicon waves. The TG solutions are recovered by expanding **B** in a power series in m_e,

$$\mathbf{B}=\exp\left(i\frac{\psi}{m_e}\right)\sum_{n=0}^{\infty}\mathbf{A}_n m_e^n, \tag{35}$$

in Eqs. (23) and (24), and equating the coefficients of each power of m_e to zero. For

$$\exp\left\{-\mathrm{Im}\left[\int_0^a \frac{k dr'}{\delta(r')}\right]\right\}\approx\exp\left\{\frac{ka}{\delta_r}\frac{\nu}{\omega}\right\}\gg 1 \tag{36}$$

the first-order result is

$$\Gamma_m(a)\rightarrow-\mu_0\frac{ia}{ka-im}\,p_m(a,a,k),$$

$$\frac{\mathbf{j}_2(r)}{j_{2,r}(a)}\rightarrow\frac{ka}{ka-im}\left\{1-\frac{im}{kr},\frac{i}{\delta},-\frac{1}{\delta}\right\}\sqrt{\frac{a}{r}\frac{n_0(r)}{n_0(a)}}$$
$$\times\exp[-i\Phi_m(k,r)], \tag{37}$$

$$\Phi_m(k,r)=\int_r^a\left[\frac{k}{\delta(r')}-\frac{k_w(r')^2}{k}-\frac{m}{2kr'}u(r')\right]dr',$$

where we represent an arbitrary vector **V** by $\{V_r,V_\phi,V_z\}$. For the plasma described by Eq. (2) the exponent in Eq. (36) is of order 1, the approximation is not valid, and the *H* and TG waves are coupled, requiring the calculations of Sec. IV for description. At higher magnetic fields and densities (e.g., $B_0=1$ kG and $n_0\simeq10^{13}$ cm^{-3}) Eq. (36) is well satisfied. Using Eq. (37) in Eqs. (33) and (34), we can make three main observations: (1) the term $\Gamma_m(a)$ has an imaginary part which is large compared to that of F_1, thereby spoiling the narrow resonances of the *H* wave; (2) the amplitude of the TG wave decays inward from the plasma edge with a skin depth of the order of $\omega\delta_r/(k\nu)$; and (3) the TG currents on the surface (j_ϕ and j_z) are larger than the radial current (j_r) by factor of order δ. Since the *H* current components are all of the same order and the radial component cancels that of the TG wave at the surface, the surface components of the current are dominated by the TG waves near the surface. In calculating the antenna plasma resistance the currents are squared and integrated. The integral of the exponential function is proportional to δ, and hence the transverse TG currents dominate the total absorption by a net factor of $1/\delta$ on the surface. This result was obtained by Shamrai *et al.*[3] in their analysis of the exact solutions for constant density. For axially peaked plasma density profiles the reduced surface density shifts the balance of heating to the helicon waves near the axis as we will see in the sequence of radial heating profiles in Fig. 14.

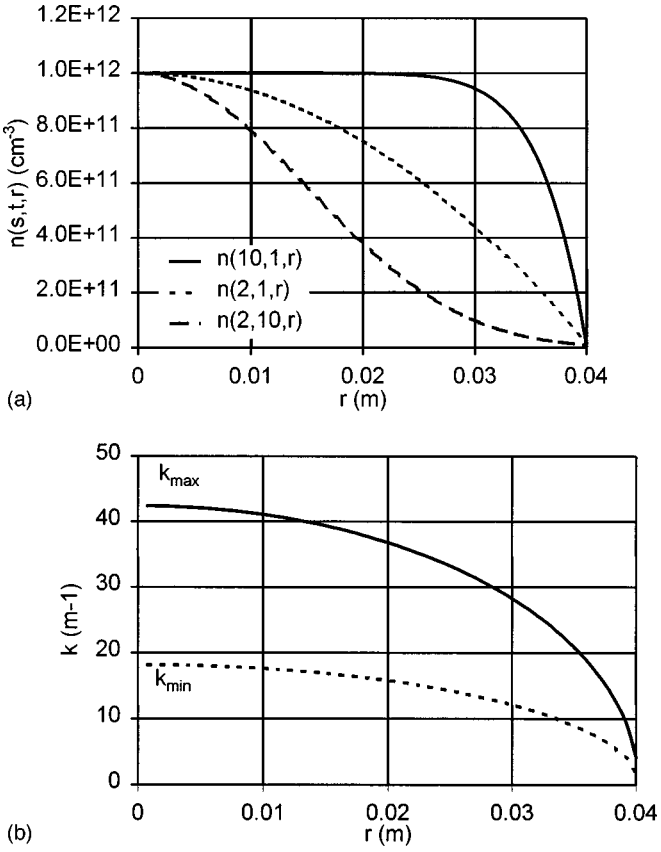

FIG. 4. (a) Three of the density profiles investigated. (b) Radial range in which helicon waves propagate in a local approximation at each k for $n_0=10^{12}$ and a parabolic density profile.

For a constant density the transverse electric helicon field solutions are also Bessel functions. We have calculated the antenna plasma resistance in that approximation for several antenna configurations, varying B_0 about 1 kG and n_0 about 10^{13} cm^{-3}. In each case the transverse electric wave number spectral resonances were significantly sharper and higher than that for the exact solution but the skirts of the resonances were lower. As a result we discerned no clear pattern of relative size of the antenna plasma resistances for the two approaches.

IV. CALCULATIONS

We explore antenna coupling for the plasma parameters of Eq. (2) using a parametrization of the density profile used earlier,[8]

$$n(s,t,r)=n_0\left[1-\left(\frac{r}{w}\right)^s\right]^t. \tag{38}$$

To avoid numerical difficulties when $n(a)=0$, w is chosen so that $n(s,t,a)=0.01n_0$. Exact Bessel function solutions are used for a constant-density profile. Some other profiles used are shown in Fig. 4(a). The $(s,t)=(2,10)$ profile is similar to a Gaussian. In Part I we learned that for a given constant density there is a range of axial wave numbers for

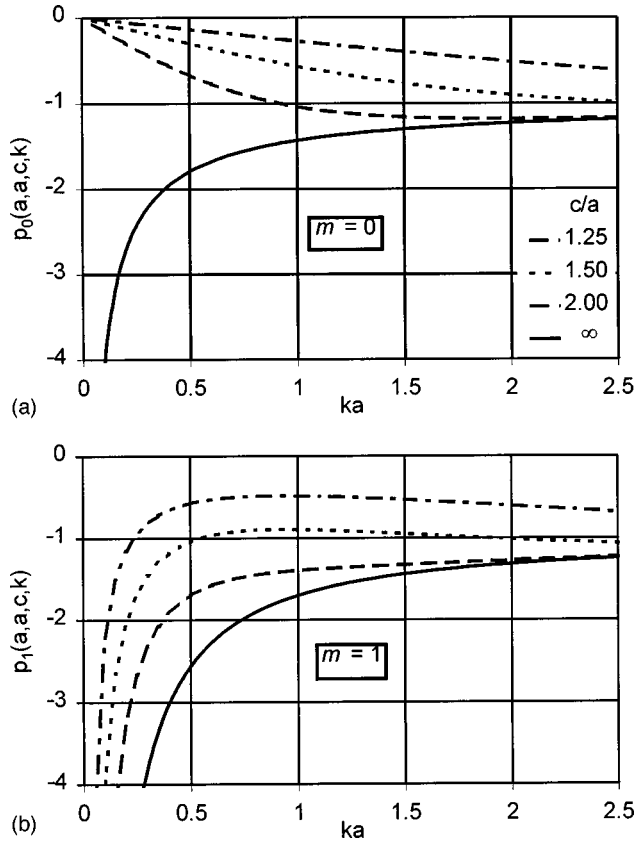

FIG. 5. The value of $p_m(a,a,c,k)$ as a function of ka for various values of c/a.

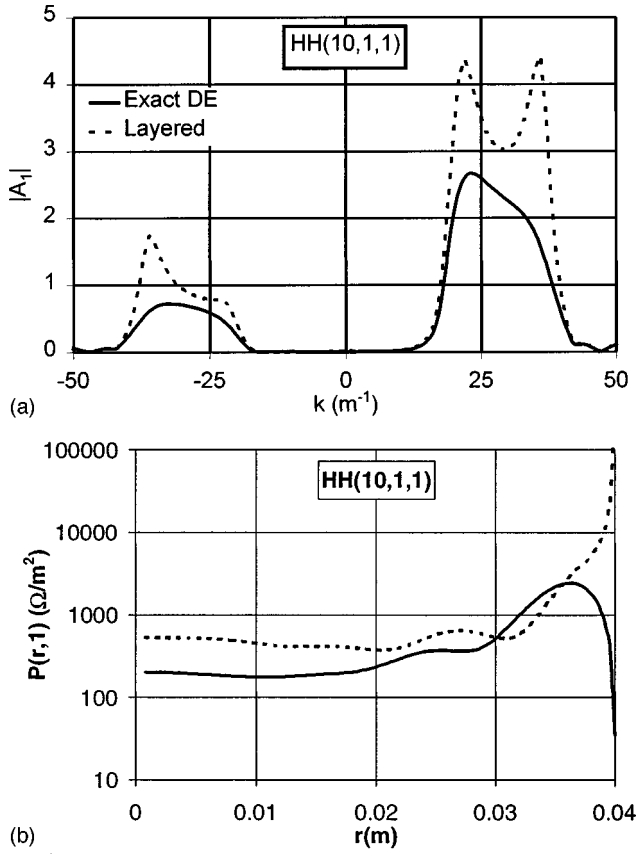

FIG. 6. Exact DE result compared with the layered result neglecting the density gradient, $u(r)$, for the $m=1$ mode excited in a plasma with a nearly square density profile by a half wavelength helical antenna: (a) helicon amplitude $|A_1|$; (b) power deposition profile $P(r,1)$.

which helicon waves can propagate. Figure 4(b) shows how the range of locally propagating k values would shrink as the density decreases with radius for a parabolic profile. For a fixed k, helicon waves can propagate for

$$r_{\min}(k)<r<r_{\max}(k), \tag{39}$$

where the limiting radii are solutions of $k_{\min}=2k_w(r)\sqrt{\delta(r)}$ and $k_{\max}=k_w(r)/\sqrt{1-\delta(r)}$. The TG waves propagate for $r>r_{\min}(k)$. The waves are strongly coupled near $r_{\min}(k)$.

The fields depend on the antenna location through the multiplicative function p_m. To simplify the results without losing the major physical effects, we now set $b=a$, so that the antenna is at the plasma boundary. The function $p_m(a,a,c,k)$ is shown in Fig. 5 for a typical range of parameters. For the cases considered, the major spectral contributions occur for $2>ka>0.8$. As long as $c/a>1.5$, we see from Fig. 5 that we may take $c/a\to\infty$ with little *qualitative* difference in the results. The examples which follow were therefore computed with $b=a$ and $c\to\infty$.

The results in the following figures are labeled with the notation XX(s,t,m), where s and t specify the density profile, m the azimuthal mode number, and XX is L for a single loop or N3, HH, or H1 for the three antennas of Fig. 3.

A. Effect of the density gradient term $u(r)$

The importance of the density-gradient terms in Eq. (24) is illustrated in Figs. 6 and 7, which compare the solutions with and without $u(r)$ for a near uniform profile HH(10,1,1) and for a parabolic profile HH(2,1,1). There are also clear differences in the spectral amplitudes of the $A_1(H)$ and A_2(TG) basis functions (not shown). The $u(r)=0$ amplitudes are larger and show a greater preference for the shorter wavelength (larger k) mode. Differences in the radial power deposition profiles are particularly pronounced, with the $u(r)=0$ solution predicting greatly increased heating of the surface. For $(s,t)=(1,0)$ the exact and $u(r)=0$ antenna plasma resistances are 1.3 and 4.6 Ω, respectively. For (2,1) they are 2.2 and 8.5 Ω, respectively, compared with experimental values of the order of 2 Ω.

B. Variation with density profile

Figures 8(a)–8(d) show the variation of spectral amplitudes through a succession of progressively more peaked density profiles corresponding to those shown in Fig. 4(a). Note that the H and TG basis functions are normalized to common values on the axis. The TG functions will often increase exponentially to the plasma surface. Since the H and TG radial currents balance at the surface, the TG amplitude A_2 must be correspondingly small. The $|A_2|$ traces in Figs. 8(a)–8(d) should therefore be interpreted with respect to shape and relative magnitude from figure to figure but not compared to the $|A_1|$ traces without further calculation. In the constant density profile case we see two peaks (for $k>0$), at $k\sim 23/m$ and $k\sim 32/m$, that are broadened to overlap

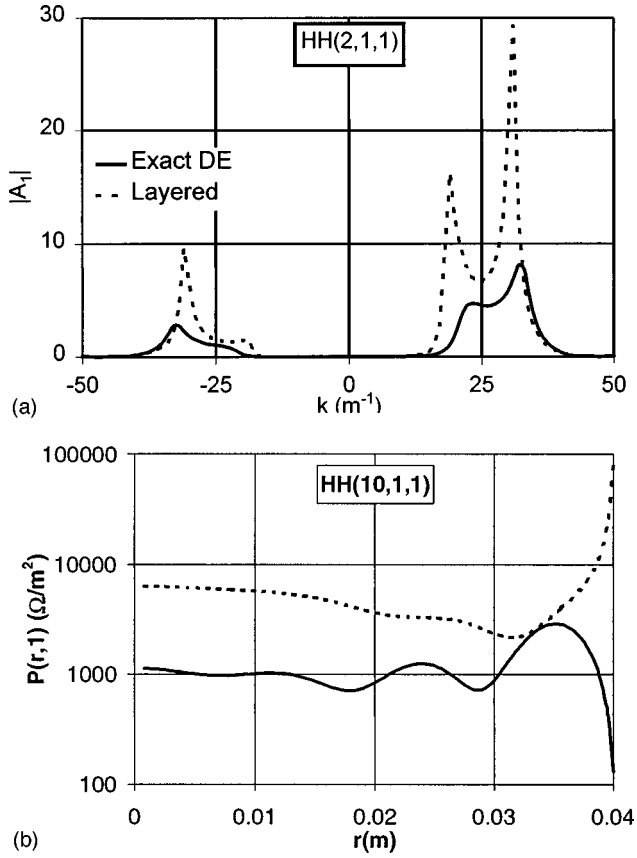

FIG. 7. The same as Fig. 6 but for a parabolic density profile.

by collisions and coupling between the waves which modify the resonant denominator. As the density becomes more peaked the amplitude of the shorter wavelength resonance increases significantly with respect to the longer one. We might anticipate this from Fig. 4(b) since, as k increases, integration of the equation for the helicon basis function employs a larger evanescent distance between $r_{\max}$ and the surface. Consequently, $j_{1,r}(a)/j_{2,r}(a)$ is reduced and hence, by Eq. (13), $|A_1(k)|$ is increased. The magnitude of the helicon basis function is reduced near the surface leading to good penetration. This effect is a variation of the antiresonance phenomenon. For all profiles the H wave amplitude exceeds the TG wave amplitude by about an order of magnitude. The TG currents are still important, however, since they are approximately proportional to $k_\perp$ times the magnetic field, and over much of the spectrum $k_\perp$ is much larger for the TG than the H wave.

In Fig. 9 the magnitudes of the azimuthal magnetic fields of H and TG waves, as well as their phased sums, are shown as a function of radius for the various density profiles shown in Fig. 5(a). They were computed for $k=32/m$, where we expect the H and TG waves to be well separated. The TG wave magnitudes are uniformly smaller than the H wave, and the TG wave decays inward from the surface for the more uniform density profiles but penetrates to the axis for the more centrally peaked profiles. To lowest approximation the fields are well represented by the H wave alone, which supports our identification of the two independent solutions (distinguished by their behavior on the axis) as H and TG

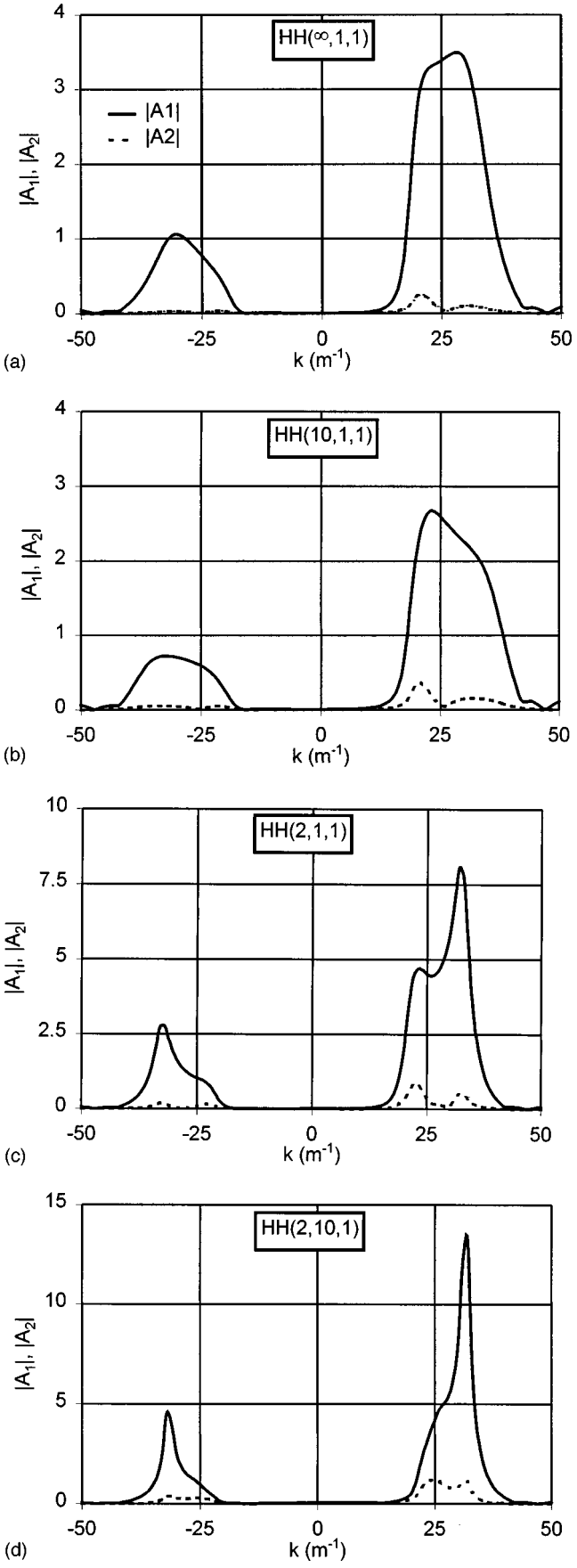

FIG. 8. Amplitude of the helicon and TG waves for density profiles which are (a) square; (b) nearly uniform; (c) parabolic; and (d) peaked.

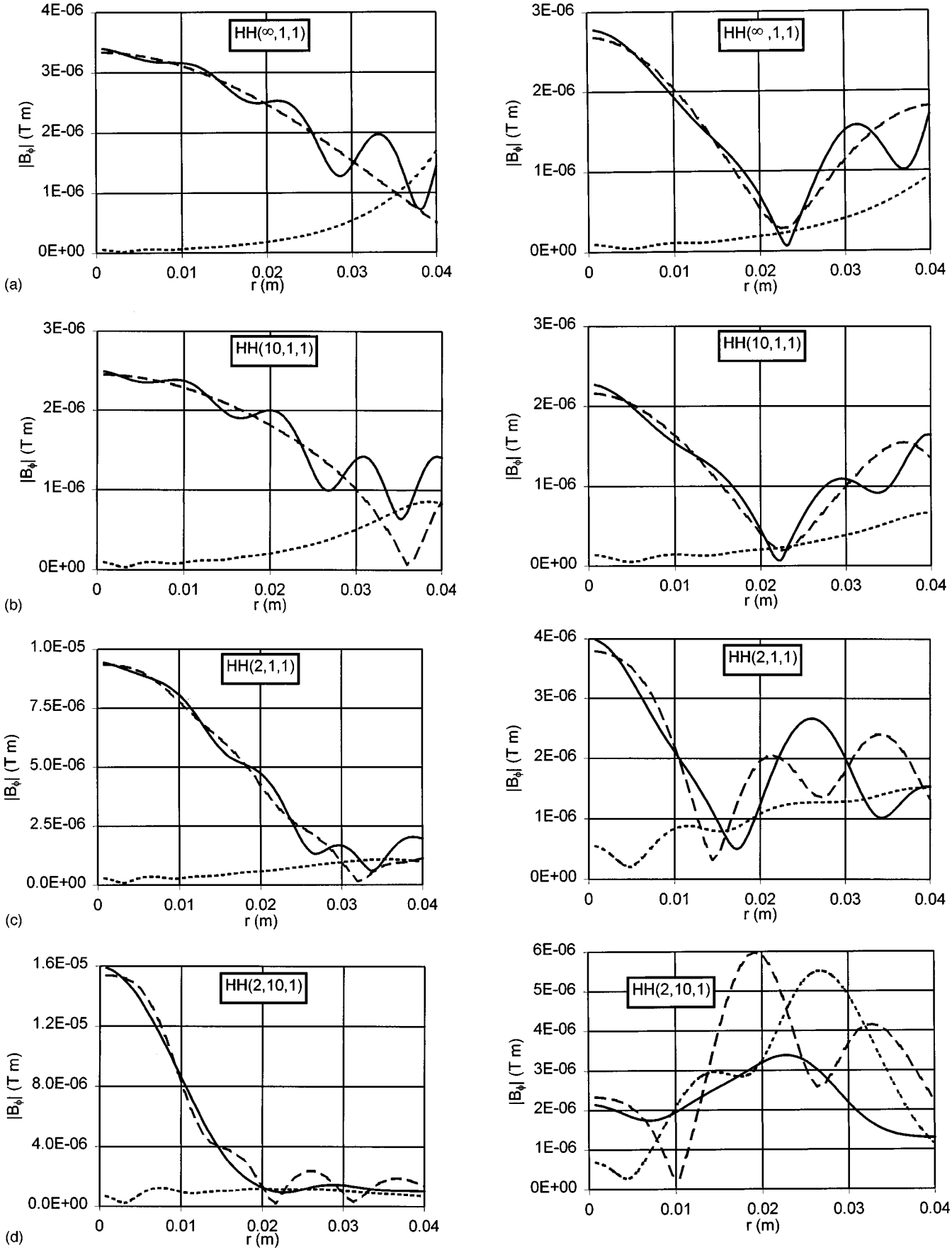

FIG. 9. Comparison of the total $|B_\phi| = |A_1 B_{1_\phi} - A_2 B_{2_\phi}|$ (—) to the H contribution $|A_1 B_{1_\phi}|$ (– – –), and the TG contribution $|A_2 B_{2_\phi}|$ (---) for $k = 32/m$, $m = 1$, and the profiles of Fig. 8.

FIG. 10. The same as Fig. 9 but for $k = 23/m$.

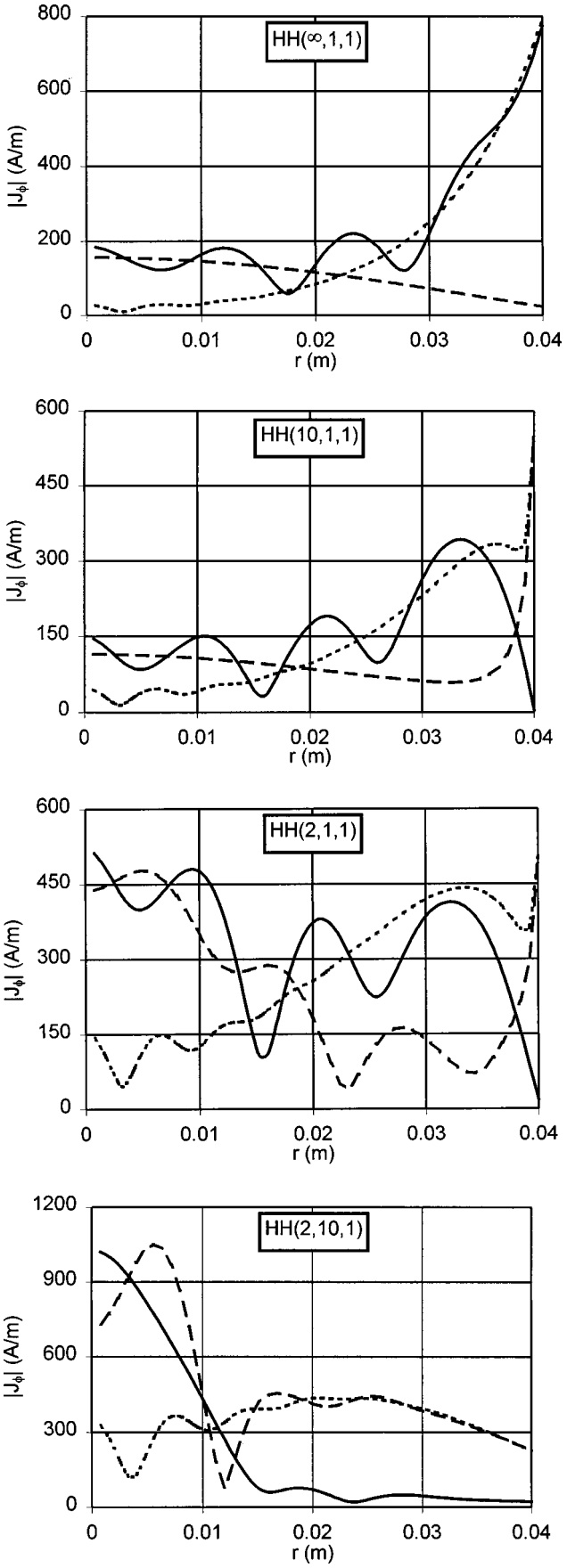

FIG. 11. The same as Fig. 9 but for $|J_\phi|$, $|A_1 J_{1_\phi}|$, and $|A_2 J_{2_\phi}|$.

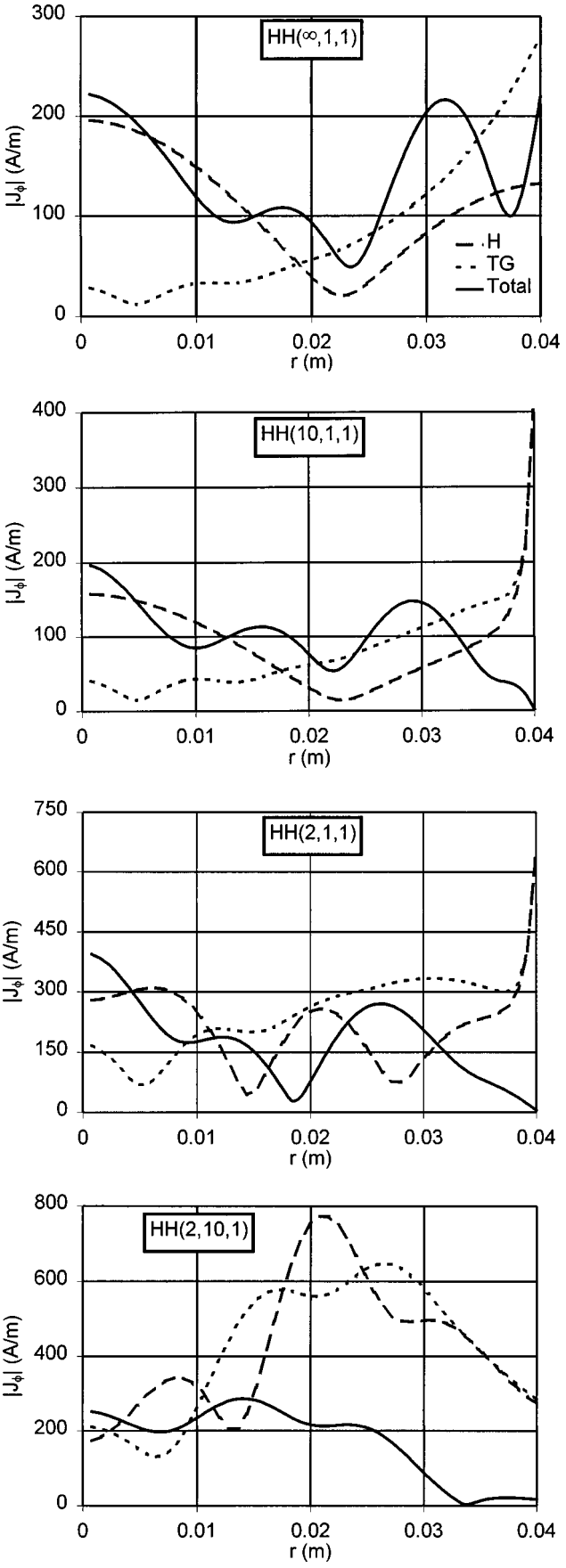

FIG. 12. The same as Fig. 11 but for $k = 23/m$.

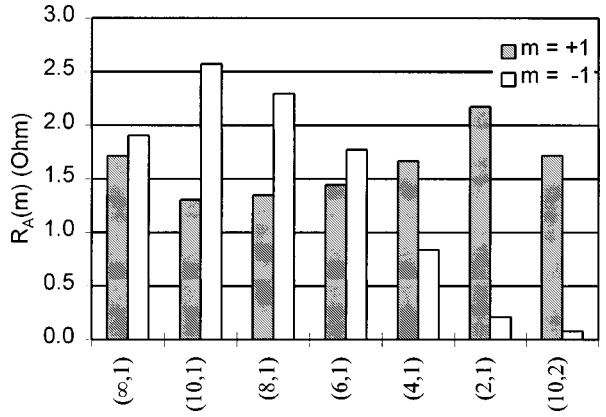

FIG. 13. The dependence of antenna plasma resistance on density profile (s,t) and wave polarization for $m=\pm 1$ shown for progressively more peaked density profiles.

waves. Oscillations of the TG waves are not directly apparent because the magnitude is plotted, but they can be seen in the perturbation of the total field. In Fig. 10 the azimuthal field magnitudes are shown for $k=23/m$ where we expect, from Fig. 4(b) and the constant density $k-\beta$ diagram discussion of Part I that the H and TG waves are strongly coupled near the axis. Indeed, for the more uniform profiles the two solutions retain the H and TG structure; but for the more centrally peaked profiles, strong coupling is apparent. In Figs. 11 and 12 we see that the magnitudes of the H and TG azimuthal currents, computed at the two spectral peaks, are comparable for all profiles. Near the surface they tend to oppose each other and leave a significantly reduced net field. Since $\mathbf{E}\propto\epsilon^{-1}\cdot\mathbf{J}$, the net electric field will also be sensitive to the presence of the TG wave.

C. Differences between $m=+1$ and $m=-1$ modes

Poor excitation of negative m modes has been observed experimentally.[10,11] Kamenski and Borg,[9] using a transverse electric analysis of a high magnetic field and high density plasma including only helicon waves, have suggested that this is due to the narrowness of realistic plasma profiles and difficulty of wave penetration. They perform a Wentzel–Kramers–Brillouin analysis and attribute the effect, at least in part, to the narrowness of the transparency region. This argument does not necessarily apply in our lower magnetic field case since the TG waves have a wider transparency region. Variation of antenna plasma resistance with profile is shown in Fig. 13 for a 20 cm HH antenna and $m=+1$ and $m=-1$ waves. There is not much variation for the $m=+1$ waves. The $m=-1$ plasma resistance is comparable to or larger than the $m=+1$ case for near uniform profiles but the plasma resistance drops significantly as the profile becomes more centrally peaked. Figure 14(a) shows the absorption profiles as a function of radius for two nearly uniform density profiles for $m=1$ and $m=-1$ waves. In the constant density case the energy deposition rises rapidly with increasing radius to a maximum at the surface. For the more realistic profiles, the density gradient term $u(r)$ and the expanded evanescent region causes a reduction of surface current and a downturn in the absorption just below the surface. The indicated antenna plasma resistances are roughly comparable. Figure 14(b) shows the absorption profiles for two more centrally peaked density profiles. As the density becomes more peaked, the absorption becomes larger on axis for the $m=1$ wave, giving an almost uniform deposition profile, while it decreases on axis for the $m=-1$ waves. To gain insight into the reasons for this, we show in Fig. 14(c) spectral antenna plasma resistances for $m=(\pm)1$ for a near uniform density profile and the $m=1$ resistance for a sharply peaked density profile. The $m=-1$ sharply peaked density resistance is too small to be seen on the same graph. For the near uniform profile, the $m=+1$ mode has a large peak at

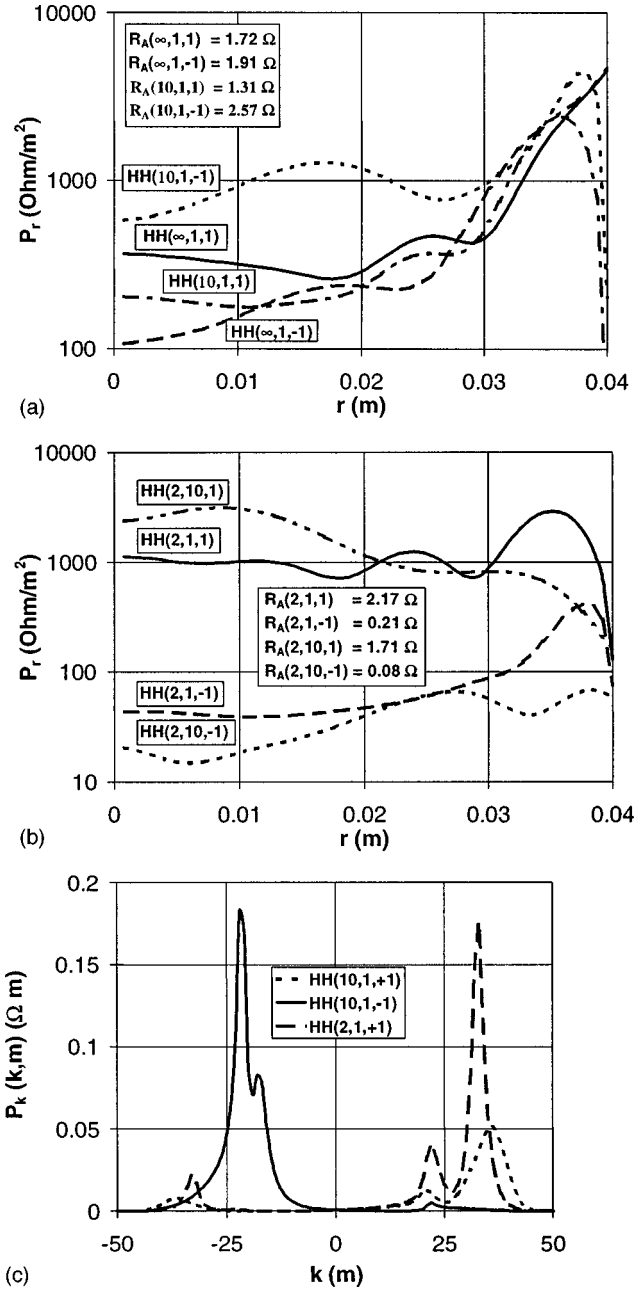

FIG. 14. The dependence of power absorption $P(r,1)$ on density profile for (a) two near uniform profiles, (b) two axially peaked profiles, and (c) spectral antenna plasma resistance for HH(10,1,+1), HH(10,1,−1), and HH(2,1,+1).

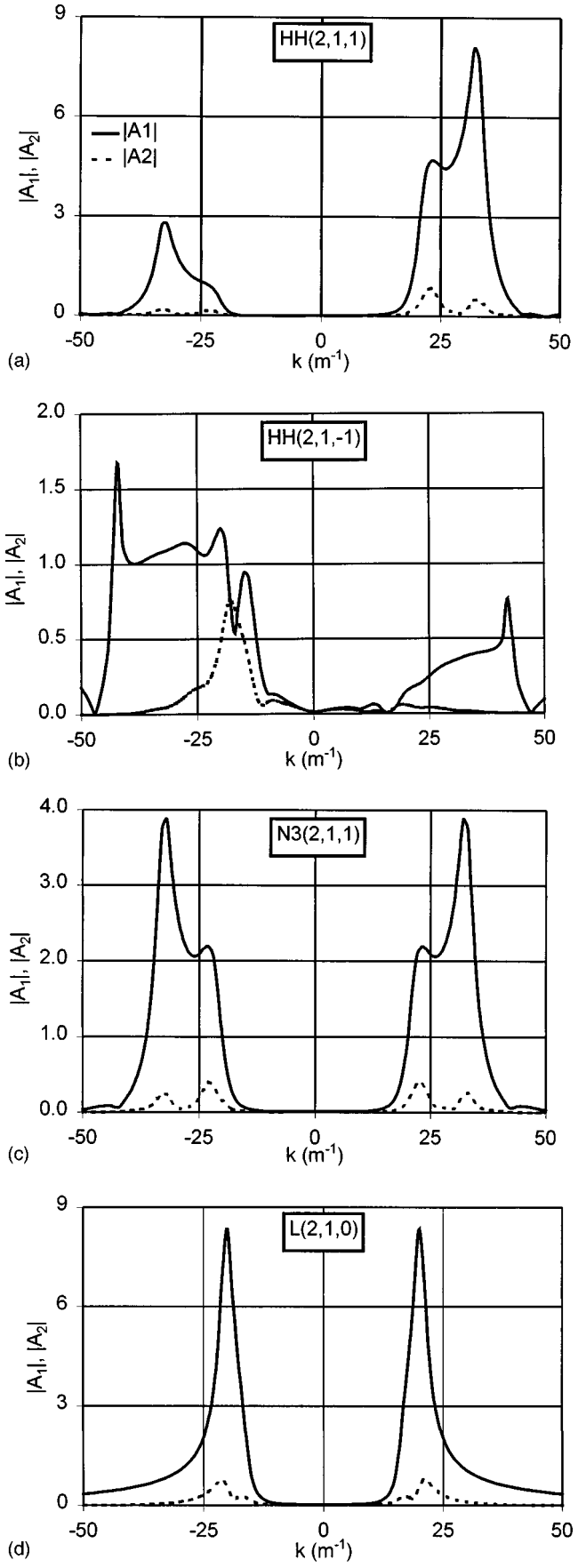

FIG. 15. The amplitudes of helicon and TG waves for a parabolic density profile for different antennas and wave polarizations.

TABLE I. Variation of antenna resistance with configuration.

Configuration	R_+ (Ω)	R_- (Ω)	R_A (Ω)
HH(2,1,1)	1.97	0.20	2.17
HH(2,1,−1)	0.01	0.20	0.21
N3(2,1,1)	0.48	0.48	0.96
L(2,1,0)	0.73	0.73	1.47

$k=36\ \mathrm{m}^{-1}$ corresponding to the lowest radial mode, and a small peak at $k=21\ \mathrm{m}^{-1}$ corresponding to the second radial mode. The $m=-1$ mode has large peaks at $k=-22\ \mathrm{m}^{-1}$ and $k=-18\ \mathrm{m}^{-1}$ and no significant peak at larger k. This is not unexpected since the $m=-1$ mode has a narrower profile than the $m=+1$ mode,[8] and therefore a larger $k_\perp$. According to the basic whistler dispersion relation [Part I, Eq. (23)], the corresponding value of k (i.e., $k_\parallel$) is therefore smaller. As discussed in Sec. IV B for $m=+1$ waves, when the density profile becomes more peaked the large k peak is increased and there is better penetration of the large k helicon fields. Since the TG field decays inward from the surface a larger net current obtains on axis and more uniform heating results. For the small k $m=-1$ peak and a more peaked density profile the fields are reduced without benefit of this antiresonance phenomena. In addition, as the density becomes more peaked for $m=-1$ the peaks shift to smaller k (as occurs in the constant density for reduced density or radius) which is less than the local $k_{\min}$ for much of the radius.

D. Variation with antennas and wave polarization

Figures 15(a)–15(d) show the magnitude of the H and TG amplitudes for a parabolic density profile and a 20 cm HH antenna with $m=\pm 1$, for a 12 cm N3 and an L antenna. These lengths were chosen to give spectral peaks at the same value of k (Fig. 3). The HH(2,1,−1) system has a much broader, lower helicon amplitude than the HH(2,1,+1) case. The N3 antenna spectrum is similar to that of the HH antenna but with reduced amplitude. The symmetric L antenna $m=0$ spectrum displays a very narrow long-wavelength resonance with an amplitude comparable to the peak of the HH(2,1,+1) resonance. The antenna plasma resistance R_A and the contribution to it from $+z$ and $-z$ propagating

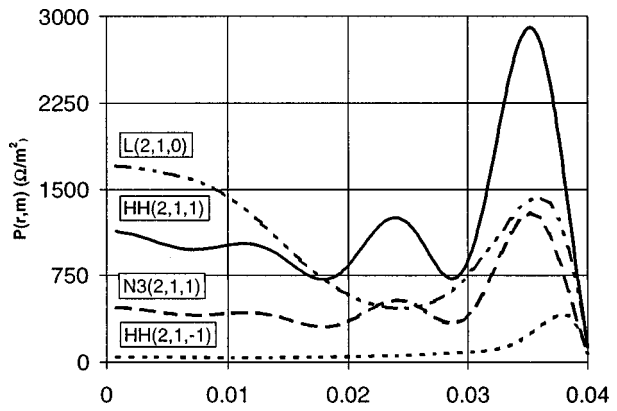

FIG. 16. Dependence of power absorption $P(r,m)$ on antenna configuration and wave polarization for a parabolic density profile.

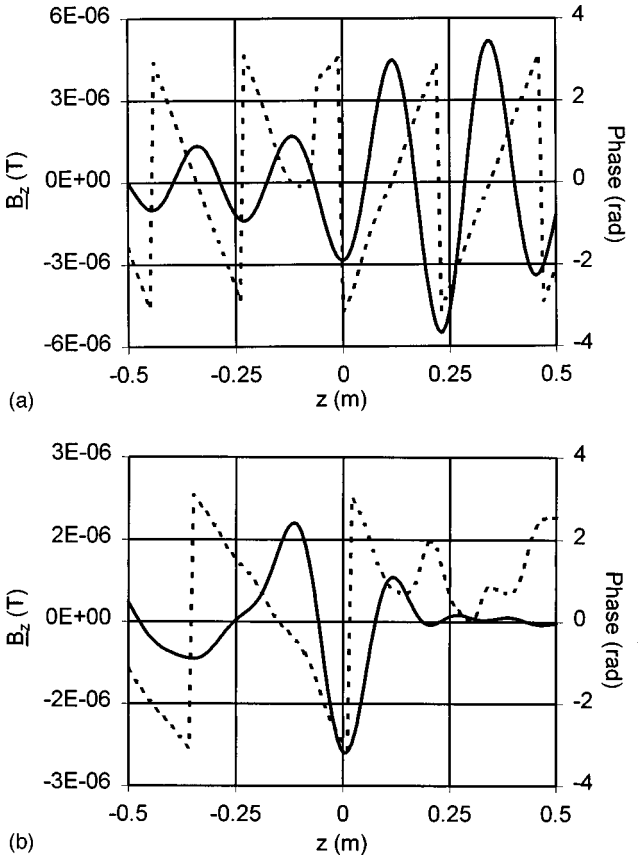

FIG. 17. Real part (—) and phase (---) of B_z at $r=1$ cm as a function of z for the (a) $m=+1$ and (b) $m=-1$ modes in a parabolic density profile.

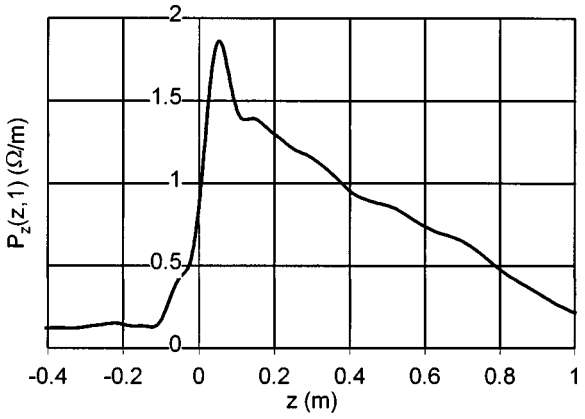

FIG. 18. Power absorbed as a function of axial distance for HH (2,1,1).

waves are given in Table I. Note that the N3 and L antennas generate equal amplitude waves propagating in the forward and back directions. The corresponding absorption profiles are shown in Fig. 16. The HH$(2,1,+1)$ antenna has the strongest coupling but the L antenna plasma resistance is only 30% smaller. However, the HH antenna delivers almost three times the power of the L antenna to waves propagating in the $+z$ direction. In contrast to the other three arrangements, the L antenna delivers a much larger fraction of its power to the center of the discharge. If power going into the $-z$ direction is not desired while taking advantage of the L antenna axial heating a solid or magnetic blocker may be used.[12]

E. Variation with *z*

Although investigation of the fields in k space is useful in developing physical models, it is necessary to invert their Fourier transforms to relate them to configuration space where measurements are made. The real part and phase of $\underline{B}_z$ as a function of z at $r=1$ cm are shown for the conditions HH$(2,1,+1)$ in Fig. 17(a) (note that the antenna is 20 cm long and centered at the origin). The real part of $\underline{B}_z$ has the appearance of a sinusoidal wave propagating away from the antenna with a greater amplitude in the $+z$ direction. Despite the broad spectrum with two sets of overlapping peaks in each direction shown in Fig. 15(a), the phase variations outside the antenna are close to linear, with measured $+z$ and $-z$ wavelengths of about 24 and 21 cm, or $k\sim+26/m$ and $-30/m$, respectively. The real part of $\underline{B}_z$ for HH$(2,1,-1)$, shown in Fig. 17(b), appears to be a damped wave propagating in the $+z$ direction, and a very long wavelength wave in the $-z$ direction. This is confirmed in the phase plot, which has a poorly defined but suggestive variation in the $+z$ direction and a linear phase variation in the $-z$ direction corresponding to $\lambda\sim40$ cm, or $k\sim16/m$. The linearity of the phase plot for $-z$ is surprising in view of the width of the spectrum shown in Fig. 15(b). Only the very long wavelength relative peaks in the H and TG spectra contribute coherently to the B_z field in real space. The power absorbed per axial length as a function of z for HH$(2,1,1)$ is shown in Fig. 18. The axial absorption is largest under the antenna, but only about 20% of the total power is absorbed there.

F. Radial wave profiles

The radial variation of the total magnetic field and its H and TG components at $z=20$ cm is shown in Fig. 19. Except near the surface, the total field follows the H field quite closely. The corresponding graphs of the currents are shown for the same location in Fig. 20. The total $\underline{J}_r$ and $\underline{J}_\phi$ are also dominated by the H wave contribution except near the surface. These results suggest a reason for the good agreement between experiments and theories which take only H waves into account. The axial component of the current shows the largest deviations, suggesting an experimental test of the contribution of TG waves.

G. Optimal antenna length

The plasma resistance as a function of HH antenna length for $m=+1$ waves and three different plasma density profiles is shown in Fig. 21(a). The optimum antenna length $L_{\rm opt}$, the value of k,$k_{\rm opt}$, for which $p_A(k,m,L)$ is a maximum, and the optimal plasma resistance $R_{\rm opt}$ is given in Table II for each profile (s,t) with density half width $a_{1/2}$: The values of $k_{\rm opt}$ are quite large compared to the average local $k_{\rm max}$. Indeed, for the more uniform profile (10,1) it is almost as large as the local $k_{\rm max}\cong42$/m for propagation on axis. The optimal coupling is weaker for the more centrally peaked profile (2,10) because of lower density on the surface where the currents are invariably large. S_k for a parabolic

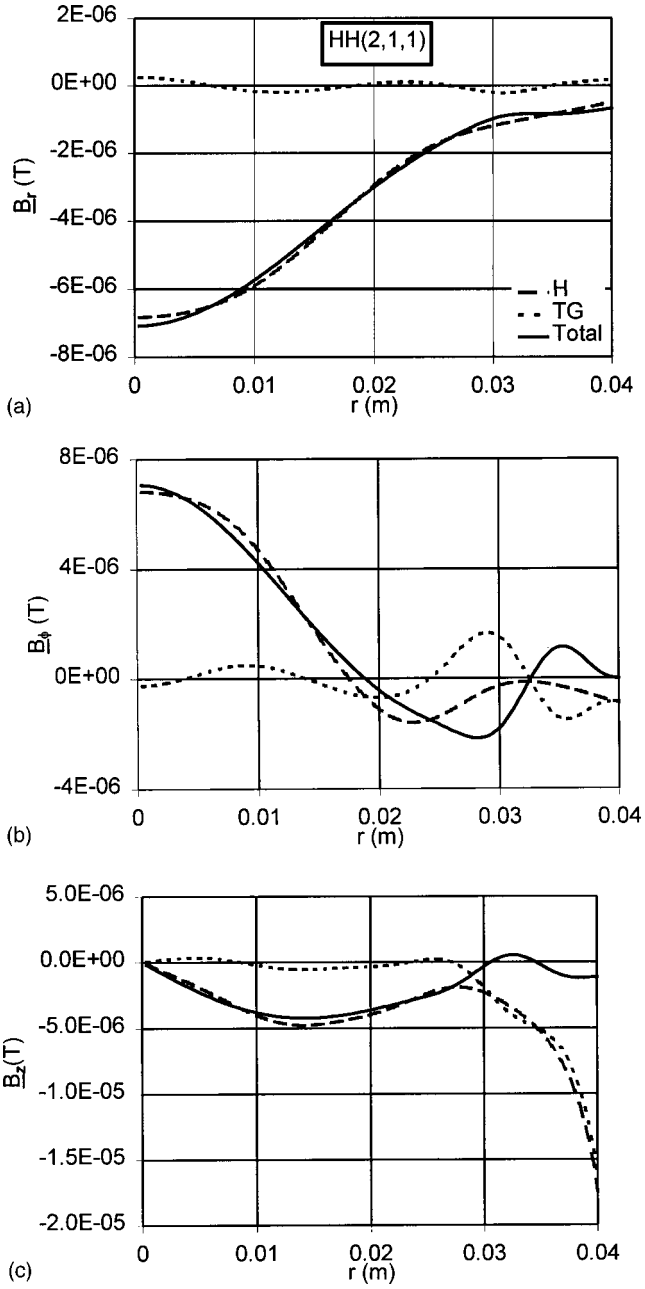

FIG. 19. Comparison of the magnetic field components and the contributions from the H and TG waves at $z=20$ cm for HH (2,1,1) for (a) B_r, (b) B_ϕ, and (c) B_z.

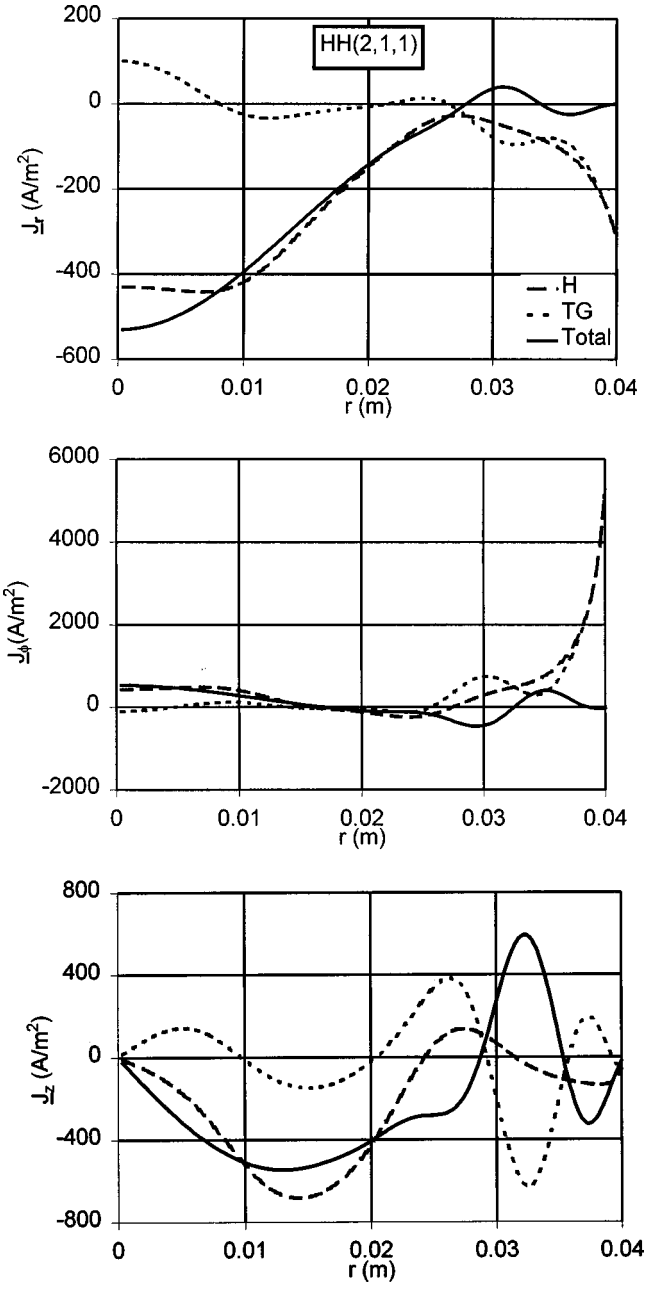

FIG. 20. The same as Fig. 19 but for the current density.

density profile is shown in Fig. 21(b), along with the p_A for an HH antenna of optimal length $L_{\text{opt}}=0.164$ cm, and for one of length $L_{m1}=0.287$ m corresponding to the first minimum of $R_A(1,L)$. Note the maximum of S_k at $k_p \cong 33/m$ which coincides with the zero of p_A for $L_{m1}=3\pi/k_p$, as well as the broad maximum of p_A for $L=L_{\text{opt}}$ which overlaps significantly with the large values of S_k at long wavelengths. The power absorption profile $P_A(r,m)$ for these two antenna lengths is shown in Fig. 21(c) where the significant relative reduction of heating is apparent. The antenna plasma resistance is shown as a function of L for the N3, HH, and H1 antennas as shown in Fig. 21(d). The respective peak resistances are 1.08, 2.57, and 6.11 Ω, showing the advantage of concentrating the antenna spectral power at the peak of the S_k.

V. SUMMARY AND CONCLUSIONS

A general expression relating the antenna current to the plasma surface fields is derived and greatly simplified by neglecting displacement currents. A fourth-order ODE is derived for coupled H and TG waves in a radially nonuniform plasma. Linearly independent solutions with short and long radial wavelengths on the axis are obtained. Results are presented for a variety of density profiles for $n_0=10^{12}$ cm^{-3} and $B_0=100$ G. For a constant density the computations reproduce the usual H and TG Bessel function solutions. They maintain their long and short wavelength character for mod-

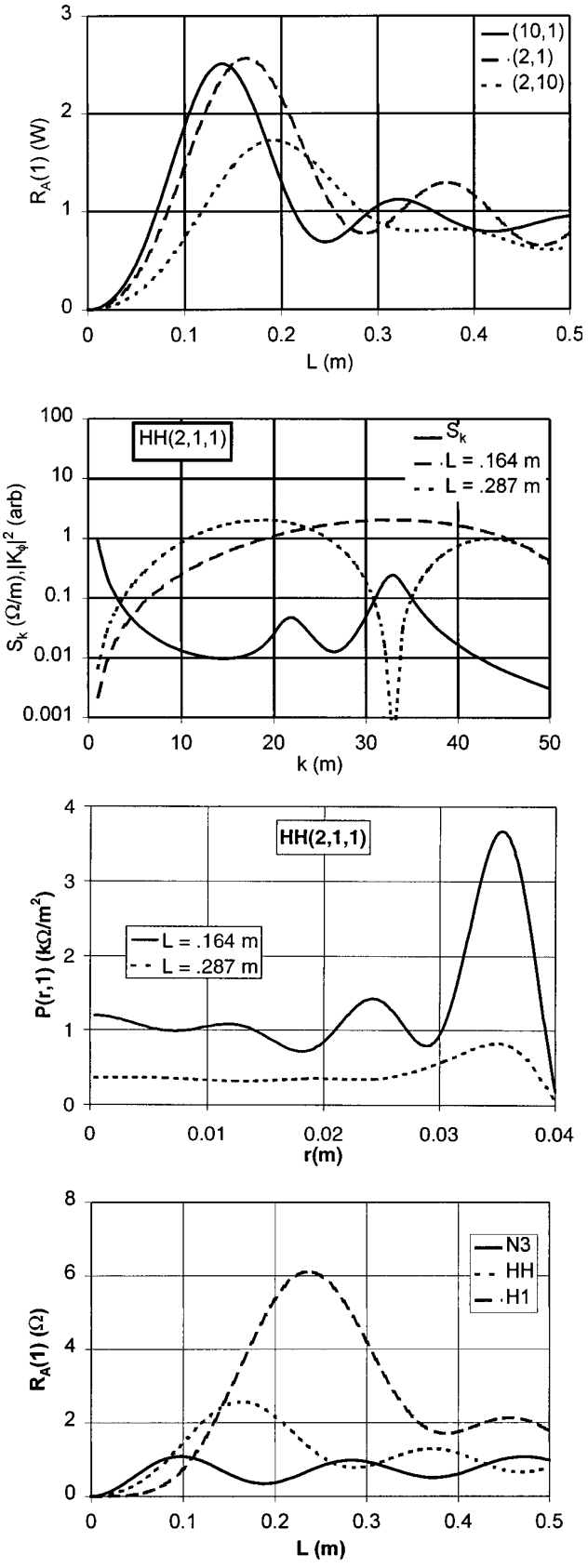

FIG. 21. (a) Plasma resistance as a function of antenna length for an HH antenna and plasmas with various density profiles (s,t), (b) specific power density S_k and antenna power spectrum for the optimal $L_{\text{opt}}=0.164$ m, and first minimal $L_{m1}=0.287$ m, antenna lengths of (a), and (c) power deposition profile for antenna lengths of (b). Variation of antenna plasma resistance with antenna length for three antennas (d).

TABLE II. Antenna optimization.

(s,t)	$a_{1/2}$ (m)	L_{opt} (m)	k_{opt} (m^{-1})	R_{opt} (Ω)
(10,1)	0.0374	0.140	38	2.51
(2,1)	0.0284	0.164	32	2.57
(2,10)	0.0170	0.190	28	1.73

erate changes in the density profile and hence may be interpreted as the extensions of H and TG waves in those cases. It is shown that layered solution methods which neglect some density gradient terms lead to an exaggeration of the antenna plasma resistance due to excess energy absorbed in a thin layer near the surface. A study of antenna types and wave polarization show major differences in the $m=+1$ spectrum, enhanced energy absorption near but not at the surface, and helical antenna performance that improves with the number of turns. A study of density profiles varying from constant to near-Gaussian shows a steady progression of increasing and narrowing of the short axial wavelength peak and reduction of the long wavelength peak. The absorption radial profile for the square density shape differs significantly from the more realistic ones. As the density profile becomes more peaked on axis, antenna plasma resistance for $m=+1$ waves varies little, but decreases significantly for $m=-1$ waves because there is no short wavelength resonance in the latter case. In configuration space, for a parabolic density profile, the wave magnetic field and current density shapes are close to that of the H field, except near the surface. However, the TG *currents* are comparable to the H currents, and hence their inclusion is critical to accurately calculating the absorption. A general discussion of the effects of TG waves at high magnetic field for a radially nonuniform plasma showed that they dominate the power absorption, in agreement with the exact result for constant density.

APPENDIX: ODE INCLUDING IONS AND DISPLACEMENT CURRENTS

To derive the general fourth-order ODE we start with Eq. (14), commute the curl with the α's, divide by α_H, and define the following coefficients which have the indicated limits for negligible displacement current and ionic effects

$$\Delta=\frac{\alpha_D-\alpha_c}{\alpha_H}=\frac{S}{D}\to\delta,\quad \Delta_0=-\frac{\alpha_C'}{\alpha_H'}\to\delta_0,$$
$$\eta_D=\frac{\alpha_D}{\alpha_H}\to 0,\quad u=\frac{\alpha_H'}{\alpha_H},\quad K_w^2=\frac{k_0^2}{\alpha_H}\to k_w^2. \tag{A1}$$

We then obtain in place of Eq. (17)

$$\Delta\nabla^2\mathbf{B}+k\nabla\times\mathbf{B}-K_w^2\mathbf{B}$$
$$=u[-\Delta_0\mathbf{r}\times(\nabla\times\mathbf{B})+i(\nabla\times\mathbf{B})_r\mathbf{z}]$$
$$-\eta_D\nabla\times[(\nabla\times\mathbf{B})_z\mathbf{z}]+(\eta_D'+u\eta_D)(\nabla\times\mathbf{B})_\phi\mathbf{z}. \tag{A2}$$

Using $\nabla\cdot\mathbf{B}=0$ in the $\mathbf{r}$ component of Eq. (A2) yields

$$B_r''=\frac{m-\Delta}{\Delta r}\,B_r'+\left(k^2+\frac{K_w^2}{\Delta}+\frac{1+m^2}{r^2}+\frac{m}{\Delta r^2}\right)B_r+\left[\frac{2m}{r^2}+\frac{1}{\Delta}\left(k^2+\frac{m^2}{r^2}\right)\right]\tilde{B}_\phi-\frac{\eta_D}{\Delta}\left(\frac{m^2}{r^2}\,B_r+\frac{m}{r}\,\tilde{B}_\phi'+\frac{m}{r^2}\,\tilde{B}_\phi\right). \tag{A3}$$

Substituting first $\mathbf{B}_z$ and then $\mathbf{B}_r''$ in the ϕ component of Eq. (A2) results in

$$(\Delta-\eta_D)\tilde{B}_\phi''=-\left[\frac{K_w^2}{\Delta}+\frac{m}{r}\,\Delta_0 u+\frac{1}{r^2}\left(m^2+\frac{m}{\Delta}-2m\right)\right]B_r-\frac{m}{r\Delta}\,B_r'+\left[k^2\,\frac{\Delta^2-1}{\Delta}+K_w^2-\frac{1}{r}\,\Delta_0 u+\frac{\Delta}{r^2}\left(1+m^2-\frac{m}{\Delta}-\frac{m^2}{\Delta^2}\right)\right]\tilde{B}_\phi'-\left[\frac{\Delta}{r}+\Delta_0 u+\frac{m}{r}\right]\tilde{B}_\phi'+\eta_D\left[\frac{m(m-\Delta)}{r^2}\,B_r+\frac{m}{r}\,(\Delta+1)B_r'+\frac{m-\Delta}{r^2}\,\tilde{B}_\phi+\frac{\Delta}{r}\,\tilde{B}_\phi'\right]. \tag{A4}$$

Although it is generally most convenient numerically to solve Eqs. (A3) and (A4) as coupled equations, they can be reduced to a single fourth-order equation for one of the field components. Taking the first and second derivative of each equation yields six linear equations from which, for example, the five quantities B_r and its derivatives may be eliminated by substitution to yield a single fourth-order equation for $\tilde{B}_\phi$.

[1] F. F. Chen and D. Arnush, Phys. Plasmas **4**, 3411 (1997).
[2] R. W. Boswell, Plasma Phys. Controlled Fusion **26**, 1147 (1984).
[3] K. P. Shamrai, V. P. Pavlenko, and V. B. Taranov, Plasma Phys. Controlled Fusion **39**, 505 (1997).
[4] F. F. Chen, Plasma Phys. Controlled Fusion **33**, 339 (1991).
[5] National Information Center Service Document No. DE85004960 (B. D. McVey, ''ICRF antenna coupling theory for a cylindrically stratified plasma,'' MIT Plasma Fusion Center Report No. PFC/RR-84-12, 1984). Copies can be ordered from the National Technical Information Service, Springfield, VA, 22161.
[6] Y. Mouzouris and J. E. Scharer, IEEE Trans. Plasma Sci. **24**, 152 (1996).
[7] F. F. Chen, M. J. Hsieh, and M. Light, Plasma Sources Sci. Technol. **3**, 49 (1994).
[8] J. D. Jackson, *Classical Electrodynamics*, 2nd ed. (Wiley, New York, 1975).
[9] I. V. Kamenski and G. G. Borg, Phys. Plasmas **3**, 4396 (1996).
[10] S. Shinohara, Y. Miyauchi, and Y. Kawai, Jpn. J. Appl. Phys., Part 1 **35**, 731 (1996).
[11] D. D. Blackwell and F. F. Chen, Plasma Sources Sci. Technol. **6**, 569 (1997).
[12] G. Chevalier and F. F. Chen, J. Vac. Sci. Technol. A **11**, 1165 (1993).